ACS Energy LETTERS

http://pubs.acs.org/journal/aelccp

Chalcocarbogels as High-Capacity and Cycle-Stable Electrode Materials for Lithium and Sodium Ion Batteries

Taohedul Islam,[○] Mengya Li,[○] Alicia Blanton, Kathryn A. Pitton, Keerthan R. Rao, Sahar Bayat, Kamila M. Wiaderek, Misganaw Adigo Weret, Subrata C Roy, Renfei Feng, Dien Li, Robiul Alam, Jing Nie, Oluwaseun Oketola, Avijit Pramanik, Beth S. Guiton, Chad Risko, Ilias Belharouak, Ruhul Amin,* and Saiful M. Islam*

Cite This: *ACS Energy Lett.* 2024, 9, 1−9

Read Online

ACCESS | Metrics & More | Article Recommendations | Supporting Information

ABSTRACT: The low capacities of commercial Li ion batteries and cycle instabilities of amorphous metal sulfide based batteries impose constraints on their utilization for large-scale energy storage. We report here the acid-free, room-temperature (RT), and solution-based synthesis of a chalcogenide−carbonaceous hybrid aerogel, termed as "chalcocarbogel", comprising molybdenum sulfide (MoS_x) and graphene oxide (GO). The chalcocarbogel is a nanoparticle-aggregated, porous, amorphous gel consisting of Mo_3S_{13} and Mo_2S_{12}-like structures as determined by synchrotron X-ray PDF, XANES, and EXAFS. The MoS_x-GO chalcocarbogel demonstrates high specific capacities of ∼1215 and ∼807 mAh g^{-1} for Li/MoS_x-GO and Na/MoS_x-GO cells, respectively, for a 50 mAg^{-1} discharge rate during the first cycle. After the activation cycles, the MoS_x-GO chalcocarbogel stabilizes, maintaining high specific capacities of approximately ∼700 mAh g^{-1} for Li/MoS_x-GO and ∼473 mAh g^{-1} for Na/MoS_x-GO cells, while continuously cycling. The MoS_x-GO aerogel reported here serves as a promising platform to develop chalcocarbogels for applications spanning both Li and Na ion batteries.

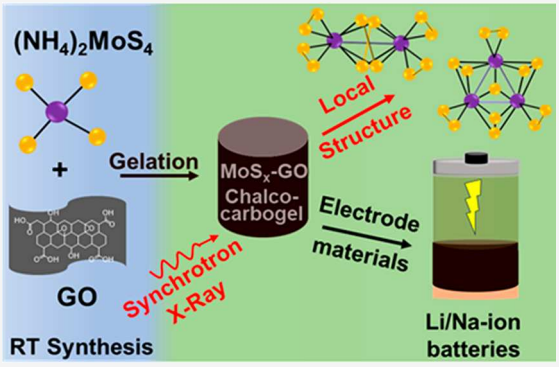

Aerogels are ultralow-density, high-surface-area, meso- to microporous materials,[1−3] composed of colloidal nanoparticles physically interlocked in three-dimensional (3D) space.[2,4,5] Apart from the traditional oxide-based gels,[6−12] the first chalcogenide-based gel, CdS, was reported by Gacoin et al.[13] Later, Brock and co-workers synthesized binary metal sulfide aerogels of CdS, PdS, CdSe, and ZnS using a thiolysis route.[4] In 2007, using the metathesis synthesis route, Kanatzidis and co-workers synthesized a large number of gels from metal sulfide or polysulfide anionic clusters and named them "chalcogels".[14−16] Chalcogels are highly disordered materials and show a wide range of applications, such as hydrodesulfurization,[17] environmental remediation,[18−20] gas separation,[14] catalysis,[21−24] and energy storage.[25]

Chalcogels, in many cases, contain high densities of polysulfides, and their −S−S− bonds can undergo chemical conversion reactions during battery charge−discharge processes, making them of interest for energy storage.[19,25] Commercial Li ion batteries (LIBs) use lithium metal oxide as the cathode and graphite as the anode, both of which make use of intercalation/deintercalation mechanisms. Unfortunately, achieving high-energy-density storage is limited due to low theoretical specific capacities.[26,27] The conversion mechanism, on the other hand, for example with the complete conversion of S_8 to Li_2S, involves 16e$^-$ ($16Li^+ + S_8 + 16e^- \rightarrow 8Li_2S$) during the charge−discharge processes and can deliver large specific capacities in sulfur-based batteries.[27−29] Chalcogels characterized with high surface areas and high porosity densities among their interconnected polysulfide-rich nanoparticles hold considerable promise as electrode materials for conversion-based rechargeable batteries.[4,25,30]

Due to high gravimetric capacity and energy density, Li sulfide batteries continue to draw substantial interest.[31] The

Received: October 5, 2023
Revised: November 11, 2023
Accepted: November 14, 2023

Downloaded via JACKSON STATE UNIV on November 30, 2023 at 21:22:37 (UTC).
See https://pubs.acs.org/sharingguidelines for options on how to legitimately share published articles.

ACS Publications © XXXX American Chemical Society

https://doi.org/10.1021/acsenergylett.3c02112
ACS Energy Lett. 2024, 9, 1−9

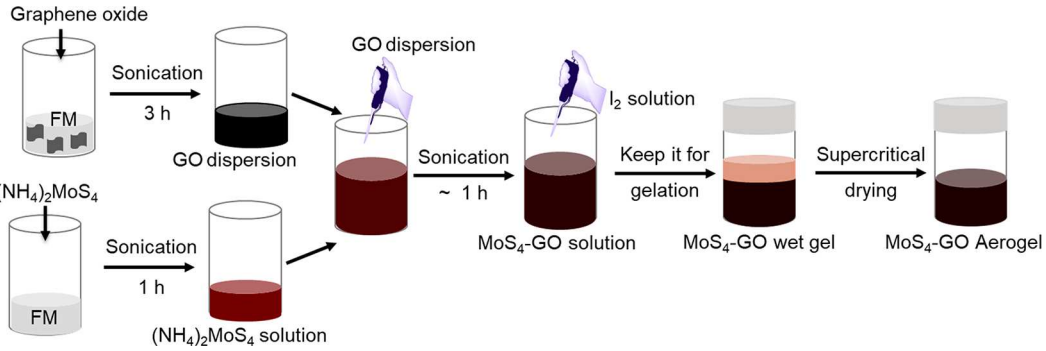

Figure 1. Schematic representation of the steps toward the synthesis of MoS_x-GO chalcocarbogel.

charge−discharge process in the cell leads to the formation of polysulfide species, A_2S_n (A= metal; n = 2−8).[27] Polysulfides tend to dissolve into the electrolyte, resulting in the loss of the active mass,[25,27,28] leading to the deterioration of specific capacity and cycle efficiencies.[32,33] Further, issues such as low electrical conductivity of S, large volumetric change during the charge−discharge process, polysulfide shuttling, formation of a nonuniform solid electrolyte interface (SEI), and dendrite growth constrain the practical application of Li sulfide batteries.[27,32] Recently Na ion batteries (SIBs) have gained attention as a promising alternative because of the high natural abundance of Na, low cost, and environmental friendliness,[34,35] and sodium sulfide batteries hold potential for large-scale energy storage applications, such as renewable energy integration and grid-level stabilization.[36,37] These materials also face several issues, however, including polysulfide dissolution and cycle instability; hence, there is a need for further development and characterization.[35,38]

Amorphous transition metal sulfides have been identified as promising electrode materials because of their high gravimetric and cycle capacities.[39−41] The gravimetric capacities for this class of materials are as high as 900−1300 mAh g^{-1} during the first discharge, though they drop precipitously in successive cycles.[39,42] Recently, we introduced chalcogels, $(MoS_4)_n$ ($n \approx \infty$) as MoS_x, as an S-equivalent high-capacity electrode for Li-sulfide batteries that show higher cyclic stability than using S alone as an electrode material.[25] This result is due to the higher affinity of the metal cation for S, which reduces the dissolution of sulfides in the electrolyte. Recent reports show that composites of carbonaceous species, such as micro-/mesoporous carbon, graphene oxide (GO), graphite, and carbon nanotubes with metal sulfides enhance the gravimetric capacity and cycle stability of Li sulfide batteries.[42−44] Based on these reports, we hypothesized that a homogeneous composite matrix of GO and metal chalcogenides in the form of a nanoparticle aggregated gel could lead to high-capacity and cycle-stable electrode materials for Li/Na ion batteries.

Here, we introduce an aerogel consisting of cross-linking between Mo−S (from MoS_4^{2-}) and GO that we have named "chalcocarbogel". The solution-processable, acid-free synthesis of the MoS_x-GO chalcocarbogels was obtained at RT and ambient pressure. We show that the integration of molybdenum sulfide anions and GO enables the homogeneity of metal sulfides and carbonaceous species across the MoS_x-GO gel particles. Moreover, the MoS_x-GO chalcocarbogels are used in Li ion and Na ion batteries that have high specific capacities and good cycle efficiencies.

The MoS_x-GO gel was synthesized from a solution of $(NH_4)_2MoS_4$, I_2, and highly dispersed GO nanosheets in formamide (FM) at RT and pressure in ∼24 h (see Figure 1 and the Supporting Information). Iodine turns into iodide and counterbalances the NH_4^+ ion, as described previously for MoS_x gel synthesis.[20] Figure 2A shows a photograph of the wet gel in an inverted vial, demonstrating the resilience of the monolith wet gel, which is typical for chalcogels.[17,20,45−47]

Scanning electron microscopy (SEM) images of the aerogel show the homogeneity of the aggregated particles (Figure 2B), while high-resolution transmission electron microscopy (HRTEM) imaging of the MoS_x-GO aerogel reveals the porosity of the gel (Figure 2C). Energy dispersive X-ray spectroscopy (EDS) in STEM confirmed the presence of C, O, Mo, and S within the aerogel (Figure 2D−I). The EDS spectrum from STEM (Figure S1) shows the overlap of S and Mo peaks at around 2.30 keV. The EDS from SEM gives the average atomic percentage (Table S1), where S is almost 4 times more abundant than Mo. Transmission electron microscopy (TEM) imaging of the MoS_x-GO aerogel shows an amorphous material with darker regions in the images indicating inclusions (Figure 2J−L). Fast Fourier transform (FFT) analysis (insets in Figure 2J−L) confirms the amorphous nature of the porous gel. The presence of pores was further evidenced by surface area measurements. The MoS_x-GO gel exhibits a type II isotherm with an H1 hysteresis loop, suggesting a porous nature;[48] the H1 hysteresis suggests mesoporosity with a very limited range of pore diameters as well as adsorption branch condensation being slowed down, and the flattened region indicates the formation of a monolayer (Figure S2).[48,49] The material has a single-point surface area of 197.82 m^2/g (at P/P_0 = 0.3) and a BET surface area of 56.64 m^2/g (Figure S2), with average adsorption and desorption pore diameters of 29.27 and 35.50 nm, respectively. The BET surface area of the MoS_x-GO aerogel is relatively low, although it can be improved through optimization of solvent exchange, degassing, and supercritical drying conditions. The thermal stability of the MoS_x-GO xerogel was analyzed by thermogravimetric analysis under a N_2 atmosphere from 25 to 580 °C (Figure S3). It showed an initial weight loss of around 5.87% up to ∼215 °C due to residual solvent evaporation from the gel preparation. From 215 to 426 °C the weight loss was about 25% because of the loss of sulfur species.[50]

XRD of MoS_x-GO demonstrates a generally featureless diffractogram, with the exception of a broad hump at ∼25° (Figure 3A). This pattern indicates the absence of long-range translational order in MoS_x-GO, confirming its amorphous nature. The Raman spectrum of MoS_x-GO reveals two peaks at

https://doi.org/10.1021/acsenergylett.3c02112
ACS Energy Lett. 2024, 9, 1−9

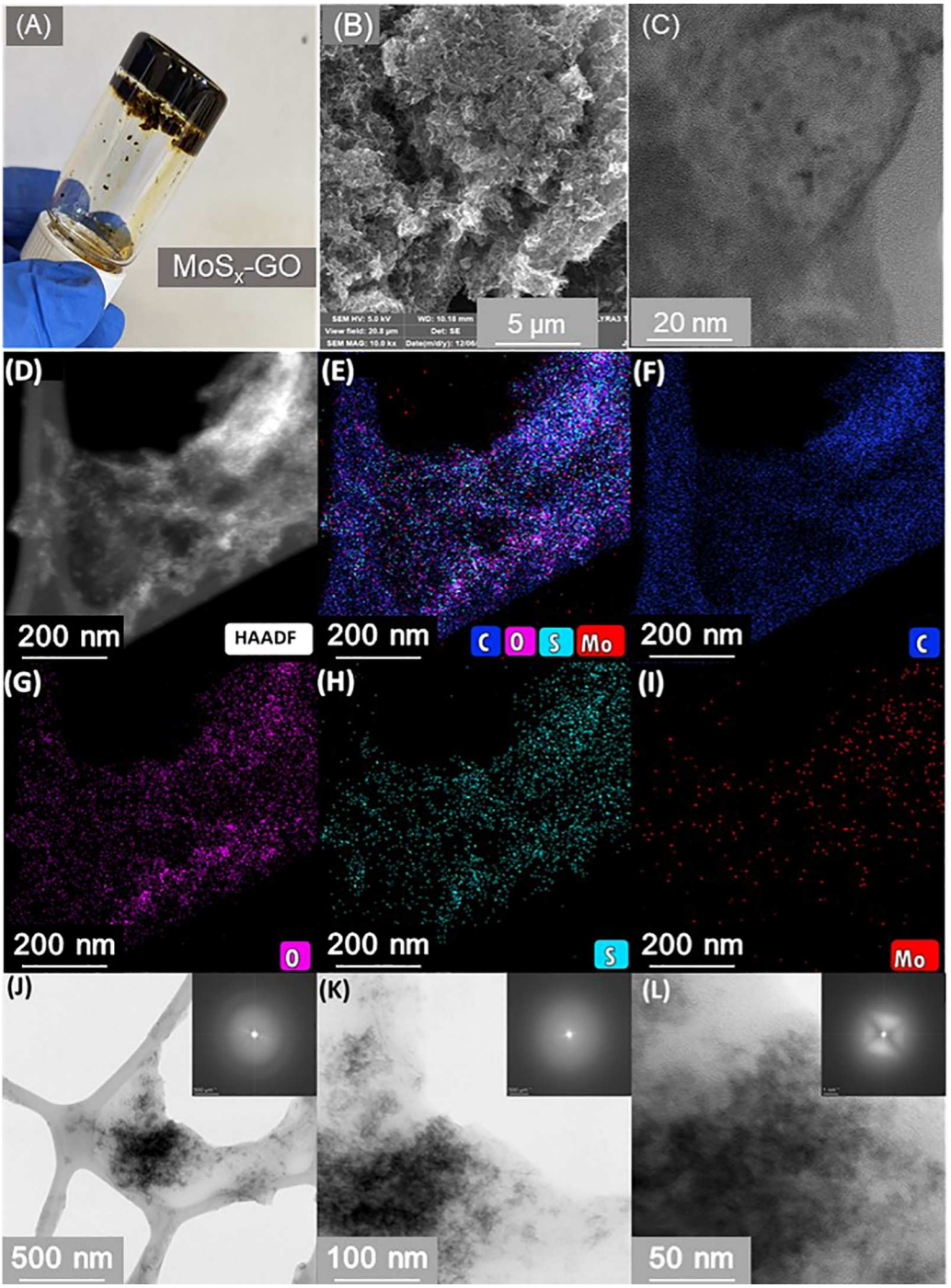

Figure 2. Photograph of an inverted vial containing MoS_x-GO wet gel, showcasing its resilience against falling apart (A). SEM image showing the aggregation of the aerogel (B). HRTEM image (C), STEM image (D), and EDS maps of the MoS_x-GO chalcocarbogel showing the distribution of each element (E−I) and elemental overlay showing the presence of Mo and S in the chalcocarbogel (E). TEM images of the same sample (J−L) with fast Fourier transforms shown as insets.

~1325.1 and ~1605.6 cm^{-1} that correspond to the graphene D and G modes of amorphous carbon, respectively (Figure 3B). The G band corresponds to in-plane vibrations of sp^2-bonded carbon atoms, while the D band is the result of out-of-plane vibrations attributed to the presence of structural defects.[39,51] Moreover, the peak at 430.5 cm^{-1} is characteristic of S−Mo_3 for the cluster anion $Mo_3S_{13}^{2-}$ as related to $(NH_4)_2Mo_3S_{13}$.[52] The peak at 501.4 cm^{-1} originates from the energy of the S−S bonding vibrations.[53] The peak around 622.8 cm^{-1} can be assigned to a C−S vibration.[50,54]

The local atomic arrangements of Mo−S in the chalcocarbogel were analyzed by synchrotron X-ray pair distribution function analysis (PDF).[55−57] The PDF result reveals the presence of atomic correlations up to ~7 Å, suggesting atomic ordering in the local structure. The absence of well-defined peaks beyond 7 Å demonstrates the lack of long-range translational symmetry, typically associated with amorphous structures (Figure 3C). This finding is consistent with the FFT and XRD results. The peak at 2.77 Å is very close to Mo−Mo distances found within crystalline $(NH_4)_2Mo_3S_{13}$

https://doi.org/10.1021/acsenergylett.3c02112
ACS Energy Lett. 2024, 9, 1−9

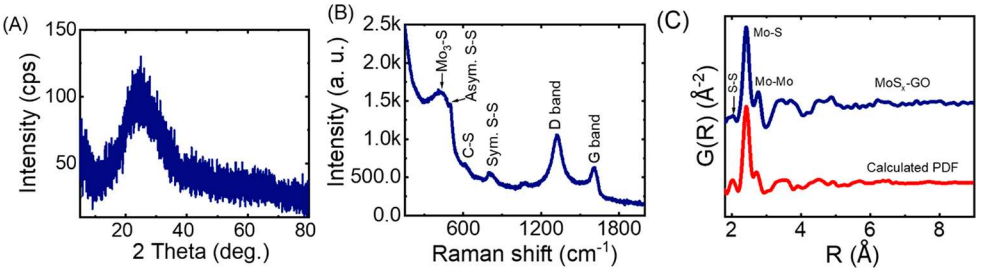

Figure 3. XRD showing the amorphous feature of the MoS_x-GO chalcocarbogel (A). Raman spectrum representing S−S and C−C symmetric and asymmetric vibrations alongside a C−S vibration (B). Pair distribution function (PDF) of the MoS_x-GO gel (blue) indicating short-range atomic ordering of the amorphous gel with the calculated PDF (red) using $Mo_3S_{13}^{2-}$ and $Mo_2S_{12}^{2-}$ clusters (C).

and $(NH_4)_2Mo_2S_{12}$.[58,59] This suggests the presence of the Mo−Mo clusters in the random network of the MoS_x-GO gel, which were absent in the precursor Mo−S material, clearly indicating the densification of MoS_4^{2-} units (Figure S4). Moreover, the PDF of the precursor $(NH_4)_2MoS_4$ exhibits Mo−S bond lengths of 2.19 Å and does not show close Mo−Mo interactions (Figure S4). In contrast, the PDF of MoS_x-GO also shows a strong peak at ∼2.41 Å that is associated with Mo−S bond distances and a small feature around ∼2.0 Å consistent with S−S interactions within crystalline $(NH_4)_2Mo_3S_{13}$ and $(NH_4)_2Mo_2S_{12}$ structures.[58,59] The presence of the peak at about 2.0 Å confirms the presence of di-/polysulfide species. The elongation of d(Mo−S) to ∼2.41 Å in MoS_x-GO can be attributed to the Mo^{6+} reduction, resulting from redox-reaction-driven polymerization of MoS_4^{2-} clusters during gelation. Hence, the reduction of Mo is attributed to the subsequent oxidations of $S^{2-} \rightarrow S^{n-}$ ($n \leq 1$). This kind of reductive polymeric condensation of MoS_4^{2-} has been observed for MoS_x chalcogels.[20] Analysis of the PDF revealed that the size of the cluster is ∼7 Å. The additional peaks below 2.0 Å can be attributed to C−C, C═C, −C═O, and −C−S distances, but their assignment is ambiguous because of the complex chemical compositions of the amorphous MoS_x-GO chalcocarbogels, as well as the surface oxidation of the chalcogels' nanoparticles, where the latter is typical for chalcogels.[55]

Quantum-chemical modeling via density functional theory (DFT) at the ωB97XD/LANL2DZ level of theory of isolated MoS_4^{2-} and $Mo_3S_{13}^{2-}$ clusters confirms the structural insights observed in the PDF (Figure S5a,c).[60−62] The DFT-determined Mo−Mo bond distance in $Mo_3S_{13}^{2-}$ is 2.71 Å, while the terminal and bridging Mo−S bond distance is 2.53 Å and the axial Mo−S bond distance is 2.46 Å (Figure S5c). For $Mo_2S_{12}^{2-}$, the DFT-derived Mo−Mo bond distance is 2.83 Å, while the terminal Mo−S bond distance is 2.51 Å and the bridging Mo−S distance varies between 2.48 and 2.59 Å (Figure S5b). The Mo−S bond distance in the MoS_4^{2-} structure is about 2.24 Å (Figure S5a). In addition, the HOMO of $Mo_2S_{12}^{2-}$ (Figure S6b) shows the presence of a d-orbital characteristic that is absent in MoS_4^{2-} and $Mo_3S_{13}^{2-}$ (Figure S6a,c). These DFT-derived bond parameters support the findings of the PDF that the lengthening of the Mo−Mo and Mo−S bond distances likely results from the reduction of Mo that is related to an increase in the coordination number of Mo.

XPS peaks at 232.4 and 229.3 eV originate from Mo $3d_{3/2}$ and Mo $3d_{5/2}$ of Mo^{4+} and the peaks at 233.8 and 229.6 eV represent the $3d_{3/2}$ and $3d_{5/2}$ of Mo^{5+}, respectively (Figure 4A), indicating the presence of both Mo^{4+} and Mo^{5+} ions in

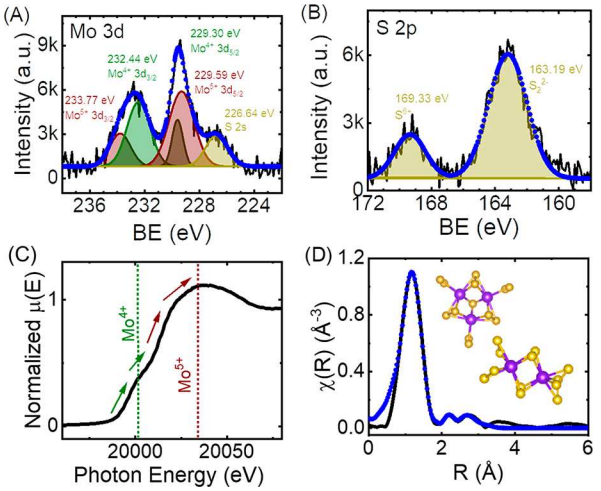

Figure 4. XPS showing different oxidation states of Mo (A) and S (B). XANES of the MoS_x-GO chalcocarbogel indicating the presence of Mo^{4+} and Mo^{5+} oxidation states (C). EXAFS fitting of MoS_x-GO by building a model spectrum with $Mo_2S_{12}^{2-}$ and $Mo_3S_{13}^{2-}$ units including a Mo−O path (D) (black line, data; blue circles, fit/model).

the MoS_x-GO chalcocarbogels.[63,64] The peaks at 226.6, 169.3, and 163.4 eV represent the S 2s and 2p orbitals, respectively (Figure 4A,B).[65,66] The strong band centered at 163.4 eV is attributed to the S_2^{2-} species.[66] Moreover, the weak peak at about 169.3 eV is related to the surface oxidation of sulfide to sulfite or sulfates, which is typical for chalcogels (Figure 4B).[67] The XPS of C 1s and O 1s reveals the C−OH, C═O, and O−C═O bonds originating from the GO present in the matrix (Figure S7A,B).[68] Further, the peak at 286.67 eV (Figure S7A) represents the C−S bond states, suggesting the linkage of the sulfide of the MoS_x species with the GO nanosheets. This observation aligns with the finding obtained by Raman spectroscopy.[50] Detailed assignments of the XPS peaks are given in Table S2.

To better understand the local coordination of Mo, we analyzed MoS_x-GO by X-ray absorption spectroscopy (XAS) (Figure 4C,D). X-ray absorption near-edge structure (XANES) (Figure 4C) shows a change in the slope of the rising edge, which may demonstrate the presence of a mixed-valence state of Mo, analogous to XPS that we discussed above.[69,70] Mo K-edge data of the extended X-ray absorption fine structure (EXAFS) for MoS_x-GO were modeled with $(NH_4)_2Mo_2S_{12}$,[58] $(NH_4)_2Mo_3S_{13}$,[63,71] and MoO_2 (Figure 4D).[72] The fitting parameters are given in Table S3. The Mo−S and Mo−Mo bonds from the $Mo_2S_{12}^{2-}$ species fitted R values of 2.62 and

https://doi.org/10.1021/acsenergylett.3c02112
ACS Energy Lett. 2024, 9, 1−9

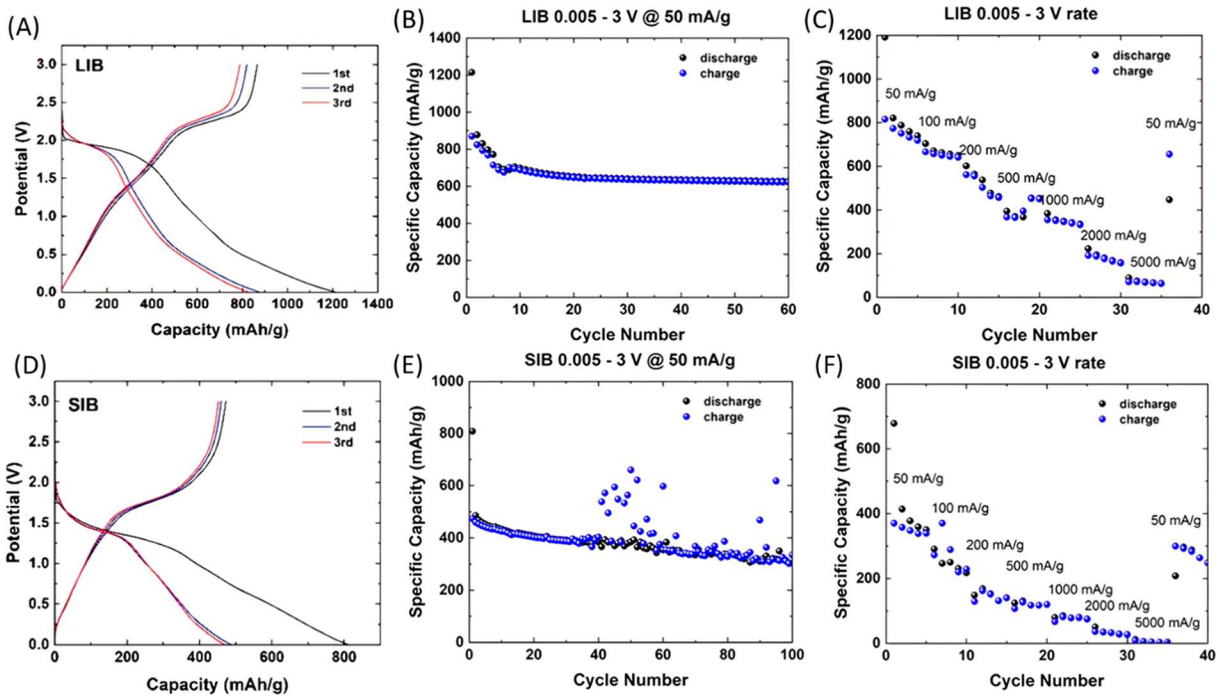

Figure 5. Galvanostatic charge/discharge profiles of MoS_x-GO electrodes in (A) LIBs and (D) SIBs half cells. (B) Cycling performance of Li/MoS_x-GO between 0.005 and 3 V @50 mAg^{-1} vs Li/Li^+. (E) Cycling performance of Na/MoS_x-GO between 0.005 and 3 V @50 mAg^{-1} vs Na/Na^+. Performance at different current rates for (C) Li/MoS_x-GO and (F) Na/MoS_x-GO.

2.87 Å, respectively, indicate the presence of Mo^{5+} in the gel. The deviation of the fitted bond distances from the pristine system is due to the phase shift and uncertainty in reference energy.[73] Further, the Mo−S and Mo−Mo bonds from $Mo_3S_{13}^{2-}$ species were observed where Mo is in a 4+ oxidation state. This result is consistent with the XPS for MoS_x-GO. The coordination numbers for the Mo−Mo bonds from both $Mo_2S_{12}^{2-}$ and $Mo_3S_{13}^{2-}$ were estimated as 2 and 3, respectively.

Overall, detailed analyses of the Raman, XPS, synchrotron X-ray PDF, XANES, and EXAFS data reveal a very complex local structure of the MoS_x-GO chalcocarbogel, which plausibly consists of both $Mo^{V}_2S_{12}^{2-}$ and $Mo^{IV}_3S_{13}^{2-}$ like species. Hence, the reduction of the Mo^{6+} ion of the precursor of $Mo^{VI}S_4^{2-}$ into Mo^{4+} and Mo^{5+} is attributed to the oxidation of the monosulfide (S^{2-}) ions to disulfide (S_2^{2-}) groups during the gelation process. Also, the presence of Mo−O bonding, as indicated by EXAFS, likely implies the linkage of molybdenum sulfide clusters with the graphene oxide moiety through S−Mo−O−C interactions. Besides, the presence of C−S, as determined by Raman spectroscopy, can be attributed to the covalent interactions of the terminal sulfides of the molybdenum sulfide cluster with C of the graphene oxide entity. In contrast to the highly intricate local structure of MoS_x-GO, the MoS_x chalcogel synthesized from the MoS_4^{2-} anion exclusively adopts the local structure featuring the $Mo_3S_{13}^{2-}$ cluster.[25] However, the structures of the MoS_x and MoS_x-GO gels are distinctly different from that of the proposed amorphous MoS_3, which is believed to have a chain-like structure consisting of Mo^{4+} ions bridged by sulfide (S^{2-}) and disulfide (S_2^{2-}) ligands.[39,74]

Galvanostatic charge−discharge experiments at constant and variable current densities were carried out using MoS_x-GO as an electrode in Li and Na ion battery half cells (Figure 5). The initial discharge capacities are ∼1215 mAh g^{-1} for a Li/MoS_x-GO cell and ∼807 mAh g^{-1} for a Na/MoS_x-GO cell. Specific capacities were determined based on the total mass of the MoS_x-GO composite. In the first few cycles, a gradual capacity loss is observed, but the largest capacity loss happens between the first and second cycles. Notably, the redox reactions of the MoS_x-GO composite include both conversion and intercalation reactions. In the initial discharge process, MoS_x/GO converted into MoS_{x-n}/GO and $n$$Li_2S$/$n$$Na_2S$ ∼1.9 V for LIBs and ∼1.38 V for SIBs. Intercalation of Li^+/Na^+ could happen within the MoS_x-GO composite, and then it formed Li_yMoS_x/Na_zMoS_x, which ultimately convert into Mo and lithium/sodium sulfides. The initial irreversibility of the MoS_x-GO electrode (Figure S8) might be attributed to the trapping of Li^+ and Na^+ in the MoS_x-GO matrix and incomplete conversion of lithium sulfide species. However, the redox reactions become reversible after the first cycle (Figure 5A,D). As evidenced by the electrochemical analysis of MoS_x-GO and also other Mo−S systems studied so far, the plausible mechanism of Li and Na storage in the MoS_x-GO composite proceeds by both conversion of MoS_x to Li/Na sulfides and Mo and intercalation of Li^+/Na^+ ions in the MoS_x-GO chalcocarbogel matrix.[75−78]

Apparently, cell polarization increases gradually upon cell cycling (Figure 5A,D and Figure S9). This increase could arise from electrolyte decomposition, which would lead to the formation of a resistive solid electrolyte interface (SEI) layer. Nonetheless, the Li/MoS_x-GO and Na/MoS_x-GO cells both exhibit a stable capacity after the activation cycles (Figure 5B,E). Li/MoS_x-GO retains a reversible discharge capacity of ∼700 mAh g^{-1}, and Na/MoS_x-GO exhibits a reversible discharge capacity of ∼473 mAh g^{-1} after 50 cycles. It is noteworthy that both the Li/MoS_x-GO and Na/MoS_x-GO cells display remarkable cyclic stability. The Na/MoS_x-GO cell shows a slightly gradual decrease in cyclic stability after the first

https://doi.org/10.1021/acsenergylett.3c02112
ACS Energy Lett. 2024, 9, 1−9

cycle, while the Li/MoS_x-GO cell delivers consistent performance after the initial cycles.

Previously reported hybrid Mo−S systems used as electrodes in LIB half cells resulted in 600−700 mAh g^{-1} specific capacity at the first discharge cycle.[75,76] The MoS_x-GO chalcocarbogel reported here exhibits a significantly higher specific capacity and a much longer cyclic stability in Li/MoS_x-GO batteries. These results underscore the crucial role played by the synergistic combination of the Mo−S and GO components in shaping distinct local structures and enhancing electrical/ionic conductivity. These factors collectively contribute to the outstanding performance achieved by these batteries. SEM post-mortem analyses were performed on cycled electrodes and compared with pristine electrodes. Although an SEI can be seen on the surface of the spent MoS_x-GO electrodes from cycled LIBs, the morphology of the MoS_x-GO is maintained after long-term cycling with no obvious cracks or disintegration (Figure S10).

Electrochemical impedance spectroscopy (EIS) measurements were performed on Li/MoS_x-GO and Na/MoS_x-GO after the 1st and 20th cycles (Figure S11B,C). Similar impedance patterns were obtained from both Li/MoS_x-GO and Na/MoS_x-GO. A comparison of individual resistance components for Li/MoS_x-GO and Na/MoS_x-GO is shown in Table S4. The distribution of relaxation time (DRT) obtained from the EIS data shows three distinguishable relaxation processes (Figure S11A). The high-frequency process is the result of charge transfer at the metal (Li or Na)/electrolyte interface (R2), while the medium-frequency process is related to charge transfer at the MoS_x-GO/electrolyte interface (R3), as the capacitance value is higher at the MoS_x-GO/electrolyte interface than at the metal (Li or Na)/electrolyte interface. The lower-frequency process originates from ionic diffusion (W_0). The resistance (R1) of ionic conductivity of the electrolyte does not appear in the relaxation process, since there is no capacitance formation. Based on the DRT information and from the Nyquist plot (Figure S11A−C), an equivalent circuit was designed (Figure S11D); the data are provided in Table S4. Both the series resistance (R1) and interfacial resistance (R2 and R3) increase in the 20th cycle compared to the 1st cycle, a result that might arise from the formation of an SEI layer. The impact of the cell resistance enhancement reflects the polarization of the charge−discharge profile where the cell polarization increases gradually. The impedance measurement substantiates the observed charge−discharge cell voltage profile.

In summary, we present the solution-processable, room-temperature, acid-free, and scalable synthesis of a MoS_x-GO chalcocarbogel. The amorphous structure of the MoS_x-GO gel was identified and analyzed by the XRD, SEM, STEM, FFT, synchrotron X-ray PDF, and XAS measurements. The local structure of the chalcocarbogel is a mixture of $Mo^{V}{}_2S_{12}{}^{2-}$ and $Mo^{IV}{}_3S_{13}{}^{2}$. Li/MoS_x-GO and Na/MoS_x-GO cells demonstrate a remarkably high specific capacity and cycle stability. In comparison to pure metal sulfide materials, the MoS_x-GO chalcocarbogel exhibits an increase in specific capacity and cycle performance.[25,79−83] This discovery underscores the significance of the interactions between Mo−S and carbon-based (e.g., GO) materials to form distinct local structures in the gel matrix, enabling promising electrode candidates for Li ion and Na ion batteries with high specific capacities and good cycle performance. MoS_x-GO can be applied as either a cathode or anode material for LIBs/SIBs depending on the selection of counter electrode materials. While the current study primarily focuses on MoS_x-GO being employed as an anode material, future work will aim to optimize the material to be paired with a high-voltage cathode to achieve stable electrochemical performance.

■ ASSOCIATED CONTENT

Supporting Information

The Supporting Information is available free of charge at https://pubs.acs.org/doi/10.1021/acsenergylett.3c02112.

Experimental methods, EDS, N_2 adsorption−desorption isotherm, PDF, TGA, DFT calculations of Mo−S clusters, XPS, dQ/dV plots for Li/MoS_x-GO and Na/MoS_x-GO cells, galvanostatic charge/discharge profile of 1st, 2nd, and 6th cycles for LIB, SEM of postcycled electrodes of LIB and SIB, DRT plot, Nyquist plots, model circuit from EIS, elemental percentage table from EDS, XPS data table, EXAFS fitting parameter table, and EIS data table (PDF)

■ AUTHOR INFORMATION

Corresponding Authors

Saiful M. Islam − *Department of Chemistry, Physics, and Atmospheric Sciences, Jackson State University, Jackson, Mississippi 39217, United States;* orcid.org/0000-0001-8518-1856; Email: muhammad.s.islam@jsums.edu

Ruhul Amin − *Electrification and Energy Infrastructures Division, Oak Ridge National Laboratory, Knoxville, Tennessee 37830, United States;* orcid.org/0000-0002-0054-3510; Email: aminr@ornl.gov

Authors

Taohedul Islam − *Department of Chemistry, Physics, and Atmospheric Sciences, Jackson State University, Jackson, Mississippi 39217, United States*

Mengya Li − *Electrification and Energy Infrastructures Division, Oak Ridge National Laboratory, Knoxville, Tennessee 37830, United States;* orcid.org/0000-0002-9581-4044

Alicia Blanton − *Department of Chemistry, Physics, and Atmospheric Sciences, Jackson State University, Jackson, Mississippi 39217, United States*

Kathryn A. Pitton − *Department of Chemistry, University of Kentucky, Lexington, Kentucky 40506-0055, United States*

Keerthan R. Rao − *Department of Chemistry, University of Kentucky, Lexington, Kentucky 40506-0055, United States; Center for Applied Energy Research, University of Kentucky, Lexington, Kentucky 40511, United States*

Sahar Bayat − *Department of Chemistry, University of Kentucky, Lexington, Kentucky 40506-0055, United States; Center for Applied Energy Research, University of Kentucky, Lexington, Kentucky 40511, United States*

Kamila M. Wiaderek − *X-ray Science Division, Advanced Photon Source, Argonne National Laboratory, Argonne, Illinois 60439, United States;* orcid.org/0000-0002-0051-3661

Misganaw Adigo Weret − *Department of Chemistry, Physics, and Atmospheric Sciences, Jackson State University, Jackson, Mississippi 39217, United States;* orcid.org/0000-0003-4891-8526

Subrata C Roy − *Department of Chemistry, Physics, and Atmospheric Sciences, Jackson State University, Jackson, Mississippi 39217, United States*
Renfei Feng − *Canadian Light Source, Saskatoon, Saskatchewan S7N 2V3, Canada;* orcid.org/0000-0001-8566-4161
Dien Li − *Savannah River National Laboratory, Aiken, South Carolina 29808, United States*
Robiul Alam − *Department of Chemistry, Physics, and Atmospheric Sciences, Jackson State University, Jackson, Mississippi 39217, United States*
Jing Nie − *Department of Chemistry, Physics, and Atmospheric Sciences, Jackson State University, Jackson, Mississippi 39217, United States*
Oluwaseun Oketola − *Department of Chemistry, Physics, and Atmospheric Sciences, Jackson State University, Jackson, Mississippi 39217, United States*
Avijit Pramanik − *Department of Chemistry, Physics, and Atmospheric Sciences, Jackson State University, Jackson, Mississippi 39217, United States;* orcid.org/0000-0002-4623-2099
Beth S. Guiton − *Department of Chemistry, University of Kentucky, Lexington, Kentucky 40506-0055, United States;* orcid.org/0000-0002-9478-9190
Chad Risko − *Department of Chemistry, University of Kentucky, Lexington, Kentucky 40506-0055, United States; Center for Applied Energy Research, University of Kentucky, Lexington, Kentucky 40511, United States;* orcid.org/0000-0001-9838-5233
Ilias Belharouak − *Electrification and Energy Infrastructures Division, Oak Ridge National Laboratory, Knoxville, Tennessee 37830, United States;* orcid.org/0000-0002-3985-0278

Complete contact information is available at: https://pubs.acs.org/10.1021/acsenergylett.3c02112

Author Contributions

○T.I. and M.L. contributed equally to this work.

Author Contributions

This manuscript was written through the contributions of all authors. All authors have given approval to the final version of the manuscript.

Notes

The authors declare no competing financial interest.

■ ACKNOWLEDGMENTS

This work was supported by the US Department of Energy's Building EPSCoR-State/National Laboratory Partnerships DE-FOA-0002624. A.B., R.A., J.N., O.O., and D.I. acknowledge the US Department of Energy's Minority Serving Institution Partnership Program (MSIPP) managed by the Savannah River National Laboratory under SRNS contract (RFP No. 0000542525 and 0000458357). S.C.R. acknowledges the NSF Division of Chemistry (NSF-2100797). This research used resources of the Advanced Photon Source, a U.S. Department of Energy (DOE) Office of Science User Facility operated for the DOE Office of Science by Argonne National Laboratory under Contract No. DE-AC02-06CH11357. The mail-in program at Beamline 11-ID-B (and/or 17-BM, 11-BM) contributed to the data. X-ray absorption spectroscopy measurements were performed at the VESPERS, Canadian Light Source, which is supported by the Canada Foundation for Innovation (CFI), the Natural Sciences and Engineering Research Council (NSERC), the National Research Council (NRC), the Canadian Institutes of Health Research (CIHR), the Government of Saskatchewan, and the University of Saskatchewan. Any use of trade, firm, or product names is for descriptive purposes only and does not imply endorsement by the U.S. Government. B.S.G. acknowledges the U.S. Department of Energy under award number DE-SC0022315. K.A.P. acknowledges the National Science Foundation CREST program Award HRD 1736136. K.A.P. and B.S.G. thank the University of Kentucky College of Arts & Sciences Expanding Transdisciplinary Research Grant. K.R.R., S.B., and C.R. acknowledge the University of Kentucky (UK) Information Technology Department and Center for Computational Sciences (CCS) for providing supercomputing resources on the Lipscomb High Performance Computing Cluster.

■ REFERENCES

(1) Hüsing, N.; Schubert, U. Aerogels—Airy Materials: Chemistry, Structure, and Properties. *Angew. Chem., Int. Ed.* **1998**, *37* (1−2), 22−45.
(2) Kistler, S. S. Coherent Expanded Aerogels and Jellies. *Nature* **1931**, *127* (3211), 741−741.
(3) Bheekhun, N.; Abu Talib, A. R.; Hassan, M. R. Aerogels in Aerospace: An Overview. *Advances in Materials Science and Engineering* **2013**, *2013*, 1−18.
(4) Mohanan, J. L.; Arachchige, I. U.; Brock, S. L. Porous Semiconductor Chalcogenide Aerogels. *Science* **2005**, *307* (5708), 397−400.
(5) Brock, S. L.; Yu, H. Chalcogenide Aerogels. In *Aerogels Handbook*; Aegerter, M. A., Leventis, N., Koebel, M. M., Eds.; Springer New York: 2011; pp 367−384. DOI: 10.1007/978-1-4419-7589-8_17.
(6) Yu, Z.; Yang, N.; Apostolopoulou-Kalkavoura, V.; Qin, B.; Ma, Z.; Xing, W.; Qiao, C.; Bergström, L.; Antonietti, M.; Yu, S. Fire-Retardant and Thermally Insulating Phenolic-Silica Aerogels. *Angew. Chem., Int. Ed.* **2018**, *57* (17), 4538−4542.
(7) Schneider, M.; Baiker, A. Titania-Based Aerogels. *Catal. Today* **1997**, *35* (3), 339−365.
(8) Krumm, M.; Pueyo, C. L.; Polarz, S. Monolithic Zinc Oxide Aerogels from Organometallic Sol-Gel Precursors. *Chem. Mater.* **2010**, *22* (18), 5129−5136.
(9) Chaput, F.; Dunn, B.; Fuqua, P.; Salloux, K. Synthesis and Characterization of Vanadium Oxide Aerogels. *J. Non-Cryst. Solids* **1995**, *188* (1−2), 11−18.
(10) Dong, W.; Dunn, B. Sol-Gel Synthesis and Characterization of Molybdenum Oxide Gels. *J. Non-Cryst. Solids* **1998**, *225*, 135−140.
(11) Teichner, S. J.; Nicolaon, G. A.; Vicarini, M. A.; Gardes, G. E. E. Inorganic Oxide Aerogels. *Adv. Colloid Interface Sci.* **1976**, *5* (3), 245−273.
(12) Zhang, L.; Chen, G.; Chen, B.; Liu, T.; Mei, Y.; Luo, X. Monolithic Germanium Oxide Aerogel with the Building Block of Nano-Crystals. *Mater. Lett.* **2013**, *104*, 41−43.
(13) Gacoin, T.; Malier, L.; Boilot, J.-P. New Transparent Chalcogenide Materials Using a Sol-Gel Process. *Chem. Mater.* **1997**, *9* (7), 1502−1504.
(14) Bag, S.; Kanatzidis, M. G. Chalcogels: Porous Metal-Chalcogenide Networks from Main-Group Metal Ions. Effect of Surface Polarizability on Selectivity in Gas Separation. *J. Am. Chem. Soc.* **2010**, *132* (42), 14951−14959.
(15) Bag, S.; Trikalitis, P. N.; Chupas, P. J.; Armatas, G. S.; Kanatzidis, M. G. Porous Semiconducting Gels and Aerogels from Chalcogenide Clusters. *Science* **2007**, *317* (5837), 490−493.
(16) Heibel, M.; Kumar, G.; Wyse, C.; Bukovec, P.; Bocarsly, A. B. Use of Sol-Gel Chemistry for the Preparation of Cyanogels as Ceramic and Alloy Precursors. *Chem. Mater.* **1996**, *8* (7), 1504−1511.

(17) Bag, S.; Gaudette, A. F.; Bussell, M. E.; Kanatzidis, M. G. Spongy Chalcogels of Non-Platinum Metals Act as Effective Hydrodesulfurization Catalysts. *Nature Chem.* **2009**, *1* (3), 217−224.
(18) Riley, B. J.; Chun, J.; Um, W.; Lepry, W. C.; Matyas, J.; Olszta, M. J.; Li, X.; Polychronopoulou, K.; Kanatzidis, M. G. Chalcogen-Based Aerogels As Sorbents for Radionuclide Remediation. *Environ. Sci. Technol.* **2013**, *47* (13), 7540−7547.
(19) Oh, Y.; Morris, C. D.; Kanatzidis, M. G. Polysulfide Chalcogels with Ion-Exchange Properties and Highly Efficient Mercury Vapor Sorption. *J. Am. Chem. Soc.* **2012**, *134* (35), 14604−14608.
(20) Subrahmanyam, K. S.; Malliakas, C. D.; Sarma, D.; Armatas, G. S.; Wu, J.; Kanatzidis, M. G. Ion-Exchangeable Molybdenum Sulfide Porous Chalcogel: Gas Adsorption and Capture of Iodine and Mercury. *J. Am. Chem. Soc.* **2015**, *137* (43), 13943−13948.
(21) Staszak-Jirkovský, J.; Malliakas, C. D.; Lopes, P. P.; Danilovic, N.; Kota, S. S.; Chang, K.-C.; Genorio, B.; Strmcnik, D.; Stamenkovic, V. R.; Kanatzidis, M. G.; Markovic, N. M. Design of Active and Stable Co-Mo-Sx Chalcogels as pH-Universal Catalysts for the Hydrogen Evolution Reaction. *Nat. Mater.* **2016**, *15* (2), 197−203.
(22) Banerjee, A.; Yuhas, B. D.; Margulies, E. A.; Zhang, Y.; Shim, Y.; Wasielewski, M. R.; Kanatzidis, M. G. Photochemical Nitrogen Conversion to Ammonia in Ambient Conditions with FeMoS-Chalcogels. *J. Am. Chem. Soc.* **2015**, *137* (5), 2030−2034.
(23) Liu, J.; Kelley, M. S.; Wu, W.; Banerjee, A.; Douvalis, A. P.; Wu, J.; Zhang, Y.; Schatz, G. C.; Kanatzidis, M. G. Nitrogenase-Mimic Iron-Containing Chalcogels for Photochemical Reduction of Dinitrogen to Ammonia. *Proc. Natl. Acad. Sci. U.S.A.* **2016**, *113* (20), 5530−5535.
(24) Ha, T. D. C.; Do, H. H.; Lee, H.; Ha, N. N.; Ha, N. T. T.; Ahn, S. H.; Oh, Y.; Kim, S. Y.; Kim, M.-G. A GO/CoMo $_3$ S $_{13}$ Chalcogel Heterostructure with Rich Catalytic Mo-S-Co Bridge Sites for the Hydrogen Evolution Reaction. *Nanoscale* **2022**, *14* (26), 9331−9340.
(25) Doan-Nguyen, V. V. T.; Subrahmanyam, K. S.; Butala, M. M.; Gerbec, J. A.; Islam, S. M.; Kanipe, K. N.; Wilson, C. E.; Balasubramanian, M.; Wiaderek, K. M.; Borkiewicz, O. J.; Chapman, K. W.; Chupas, P. J.; Moskovits, M.; Dunn, B. S.; Kanatzidis, M. G.; Seshadri, R. Molybdenum Polysulfide Chalcogels as High-Capacity, Anion-Redox-Driven Electrode Materials for Li-Ion Batteries. *Chem. Mater.* **2016**, *28* (22), 8357−8365.
(26) Wang, G.; Yu, M.; Feng, X. Carbon Materials for Ion-Intercalation Involved Rechargeable Battery Technologies. *Chem. Soc. Rev.* **2021**, *50* (4), 2388−2443.
(27) Manthiram, A.; Fu, Y.; Chung, S.-H.; Zu, C.; Su, Y.-S. Rechargeable Lithium-Sulfur Batteries. *Chem. Rev.* **2014**, *114* (23), 11751−11787.
(28) Rosenman, A.; Markevich, E.; Salitra, G.; Aurbach, D.; Garsuch, A.; Chesneau, F. F. Review on Li-Sulfur Battery Systems: An Integral Perspective. *Adv. Energy Mater.* **2015**, *5* (16), 1500212.
(29) Zhong, Y.; Wang, Q.; Bak, S.-M.; Hwang, S.; Du, Y.; Wang, H. Identification and Catalysis of the Potential-Limiting Step in Lithium-Sulfur Batteries. *J. Am. Chem. Soc.* **2023**, *145* (13), 7390−7396.
(30) Bag, S.; Arachchige, I. U.; Kanatzidis, M. G. Aerogels from Metal Chalcogenides and Their Emerging Unique Properties. *J. Mater. Chem.* **2008**, *18* (31), 3628.
(31) Manthiram, A.; Fu, Y.; Su, Y.-S. Challenges and Prospects of Lithium-Sulfur Batteries. *Acc. Chem. Res.* **2013**, *46* (5), 1125−1134.
(32) Ji, X.; Nazar, L. F. Advances in Li-S Batteries. *J. Mater. Chem.* **2010**, *20* (44), 9821.
(33) Diao, Y.; Xie, K.; Xiong, S.; Hong, X. Insights into Li-S Battery Cathode Capacity Fading Mechanisms: Irreversible Oxidation of Active Mass during Cycling. *J. Electrochem. Soc.* **2012**, *159* (11), A1816−A1821.
(34) Chayambuka, K.; Mulder, G.; Danilov, D. L.; Notten, P. H. L. From Li-Ion Batteries toward Na-Ion Chemistries: Challenges and Opportunities. *Adv. Energy Mater.* **2020**, *10* (38), 2001310.
(35) Goikolea, E.; Palomares, V.; Wang, S.; Larramendi, I. R.; Guo, X.; Wang, G.; Rojo, T. Na-Ion Batteries—Approaching Old and New Challenges. *Adv. Energy Mater.* **2020**, *10* (44), 2002055.
(36) Luo, W.; Shen, F.; Bommier, C.; Zhu, H.; Ji, X.; Hu, L. Na-Ion Battery Anodes: Materials and Electrochemistry. *Acc. Chem. Res.* **2016**, *49* (2), 231−240.
(37) Hirsh, H. S.; Li, Y.; Tan, D. H. S.; Zhang, M.; Zhao, E.; Meng, Y. S. Sodium-Ion Batteries Paving the Way for Grid Energy Storage. *Adv. Energy Mater.* **2020**, *10* (32), 2001274.
(38) Hasa, I.; Mariyappan, S.; Saurel, D.; Adelhelm, P.; Koposov, A. Y.; Masquelier, C.; Croguennec, L.; Casas-Cabanas, M. Challenges of Today for Na-Based Batteries of the Future: From Materials to Cell Metrics. *J. Power Sources* **2021**, *482*, 228872.
(39) Ye, H.; Ma, L.; Zhou, Y.; Wang, L.; Han, N.; Zhao, F.; Deng, J.; Wu, T.; Li, Y.; Lu, J. Amorphous MoS3 as the Sulfur-Equivalent Cathode Material for Room-Temperature Li-S and Na-S Batteries. *Proc. Natl. Acad. Sci. U.S.A.* **2017**, *114* (50), 13091−13096.
(40) Wang, A.; Zhang, X.; Gao, S.; Zhao, C.; Kuang, S.; Lu, S.; Niu, J.; Wang, G.; Li, W.; Chen, D.; Zhang, H.; Zhou, X.; Zhang, S.; Zhang, B.; Wang, W. Fast-Charging Zn-Air Batteries with Long Lifetime Enabled by Reconstructed Amorphous Multi-Metallic Sulfide. *Adv. Mater.* **2022**, *34* (49), 2204247.
(41) Sakuda, A.; Taguchi, N.; Takeuchi, T.; Kobayashi, H.; Sakaebe, H.; Tatsumi, K.; Ogumi, Z. Amorphous Niobium Sulfides as Novel Positive-Electrode Materials. *ECS Electrochemistry Letters* **2014**, *3* (7), A79−A81.
(42) Jin, R.; Jiang, Y.; Li, G.; Meng, Y. Amorphous Carbon Coated Multiwalled Carbon Nanotubes@transition Metal Sulfides Composites as High Performance Anode Materials for Lithium Ion Batteries. *Electrochim. Acta* **2017**, *257*, 20−30.
(43) Gan, T.; Wang, J.; Liao, Y.; Lin, Z.; Wu, F. Catalytic Performance of Binary Transition Metal Sulfide FeCoS2/rGO for Lithium-Sulfur Batteries. *J. Solid State Electrochem* **2023**, *27* (4), 1045−1053.
(44) Yin, D.; Huang, G.; Zhang, F.; Qin, Y.; Na, Z.; Wu, Y.; Wang, L. Coated/Sandwiched rGO/CoS $_x$ Composites Derived from Metal-Organic Frameworks/GO as Advanced Anode Materials for Lithium-Ion Batteries. *Chem. Eur. J.* **2016**, *22* (4), 1467−1474.
(45) Oh, Y.; Bag, S.; Malliakas, C. D.; Kanatzidis, M. G. Selective Surfaces: High-Surface-Area Zinc Tin Sulfide Chalcogels. *Chem. Mater.* **2011**, *23* (9), 2447−2456.
(46) Polychronopoulou, K.; Malliakas, C. D.; He, J.; Kanatzidis, M. G. Selective Surfaces: Quaternary Co(Ni)MoS-Based Chalcogels with Divalent (Pb2+, Cd2+, Pd2+) and Trivalent (Cr3+, Bi3+) Metals for Gas Separation. *Chem. Mater.* **2012**, *24* (17), 3380−3392.
(47) Subrahmanyam, K. S.; Malliakas, C. D.; Islam, S. M.; Sarma, D.; Wu, J.; Kanatzidis, M. G. High-Surface-Area Antimony Sulfide Chalcogels. *Chem. Mater.* **2016**, *28* (21), 7744−7749.
(48) Thommes, M.; Kaneko, K.; Neimark, A. V.; Olivier, J. P.; Rodriguez-Reinoso, F.; Rouquerol, J.; Sing, K. S. W. Physisorption of Gases, with Special Reference to the Evaluation of Surface Area and Pore Size Distribution (IUPAC Technical Report). *Pure Appl. Chem.* **2015**, *87* (9−10), 1051−1069.
(49) Kumar, S.; Malik, M.M.; Purohit, R. Synthesis of High Surface Area Mesoporous Silica Materials Using Soft Templating Approach. *Materials Today: Proceedings* **2018**, *5* (2), 4128−4133.
(50) Weret, M. A.; Jeffrey Kuo, C.-F.; Zeleke, T. S.; Beyene, T. T.; Tsai, M.-C.; Huang, C.-J.; Berhe, G. B.; Su, W.-N.; Hwang, B.-J. Mechanistic Understanding of the Sulfurized-Poly(Acrylonitrile) Cathode for Lithium-Sulfur Batteries. *Energy Storage Materials* **2020**, *26*, 483−493.
(51) Li, F.; Zhang, L.; Li, J.; Lin, X.; Li, X.; Fang, Y.; Huang, J.; Li, W.; Tian, M.; Jin, J.; Li, R. Synthesis of Cu-MoS2/rGO Hybrid as Non-Noble Metal Electrocatalysts for the Hydrogen Evolution Reaction. *J. Power Sources* **2015**, *292*, 15−22.
(52) Shafaei-Fallah, M.; Rothenberger, A.; Katsoulidis, A. P.; He, J.; Malliakas, C. D.; Kanatzidis, M. G. Extraordinary Selectivity of CoMo3S13 Chalcogel for C2H6 and CO2 Adsorption. *Adv. Mater.* **2011**, *23* (42), 4857−4860.
(53) Van Wart, H. E.; Lewis, A.; Scheraga, H. A.; Saeva, F. D. Disulfide Bond Dihedral Angles from Raman Spectroscopy. *Proc. Natl. Acad. Sci. U.S.A.* **1973**, *70* (9), 2619−2623.

(54) Frey, M.; Zenn, R. K.; Warneke, S.; Müller, K.; Hintennach, A.; Dinnebier, R. E.; Buchmeiser, M. R. Easily Accessible, Textile Fiber-Based Sulfurized Poly(Acrylonitrile) as Li/S Cathode Material: Correlating Electrochemical Performance with Morphology and Structure. *ACS Energy Lett.* **2017**, *2* (3), 595−604.
(55) Terban, M. W.; Billinge, S. J. L. Structural Analysis of Molecular Materials Using the Pair Distribution Function. *Chem. Rev.* **2022**, *122* (1), 1208−1272.
(56) Chupas, P. J.; Qiu, X.; Hanson, J. C.; Lee, P. L.; Grey, C. P.; Billinge, S. J. L. Rapid-Acquisition Pair Distribution Function (RA-PDF) Analysis. *J. Appl. Crystallogr.* **2003**, *36* (6), 1342−1347.
(57) Juhás, P.; Davis, T.; Farrow, C. L.; Billinge, S. J. L. PDFgetX3: A Rapid and Highly Automatable Program for Processing Powder Diffraction Data into Total Scattering Pair Distribution Functions. *J. Appl. Crystallogr.* **2013**, *46* (2), 560−566.
(58) Mueller, A.; Nolte, W. O.; Krebs, B. (NH4)2[(S2)2Mo(S2)-2Mo(S2)2].2H2O, a Novel Sulfur-Rich Coordination Compound with Two Nonequivalent Complex Anions Having the Same Point Group but Different Structures: Crystal and Molecular Structures. *Inorg. Chem.* **1980**, *19* (9), 2835−2836.
(59) Müller, A.; Sarkar, S.; Bhattacharyya, R. G.; Pohl, S.; Dartmann, M. Directed Synthesis of [Mo3S13]2-, an Isolated Cluster Containing Sulfur Atoms in Three Different States of Bonding. *Angewandte Chemie International Edition in English* **1978**, *17* (7), 535−535.
(60) Hay, P. J.; Wadt, W. R. *Ab Initio* Effective Core Potentials for Molecular Calculations. Potentials for the Transition Metal Atoms Sc to Hg. *J. Chem. Phys.* **1985**, *82* (1), 270−283.
(61) Chai, J.-D.; Head-Gordon, M. Long-Range Corrected Hybrid Density Functionals with Damped Atom-Atom Dispersion Corrections. *Phys. Chem. Chem. Phys.* **2008**, *10* (44), 6615.
(62) Dunning, T. H.; Hay, P. J.; Schaefer, H. F. Methods of Electronic Structure Theory. *Modern theoretical chemistry* **1977**, *3*, 1−27.
(63) Islam, S. M.; Sangwan, V. K.; Li, Y.; Kang, J.; Zhang, X.; He, Y.; Zhao, J.; Murthy, A.; Ma, S.; Dravid, V. P.; Hersam, M. C.; Kanatzidis, M. G. Abrupt Thermal Shock of $(NH_4)_2Mo_3S_{13}$ Leads to Ultrafast Synthesis of Porous Ensembles of MoS_2 Nanocrystals for High Gain Photodetectors. *ACS Appl. Mater. Interfaces* **2018**, *10* (44), 38193−38200.
(64) Islam, S. M.; Subrahmanyam, K. S.; Malliakas, C. D.; Kanatzidis, M. G. One-Dimensional Molybdenum Thiochlorides and Their Use in High Surface Area MoS_x Chalcogels. *Chem. Mater.* **2014**, *26* (17), 5151−5160.
(65) Islam, S. M.; Malliakas, C. D.; Sarma, D.; Maloney, D. C.; Stoumpos, C. C.; Kontsevoi, O. Y.; Freeman, A. J.; Kanatzidis, M. G. Direct Gap Semiconductors $Pb_2BiS_2I_3$, $Sn_2BiS_2I_3$, and Sn_2BiSI_5. *Chem. Mater.* **2016**, *28* (20), 7332−7343.
(66) Islam, S. M.; Vanishri, S.; Li, H.; Stoumpos, C. C.; Peters, J. A.; Sebastian, M.; Liu, Z.; Wang, S.; Haynes, A. S.; Im, J.; Freeman, A. J.; Wessels, B.; Kanatzidis, M. G. $Cs_2Hg_3S_4$: A Low-Dimensional Direct Bandgap Semiconductor. *Chem. Mater.* **2015**, *27* (1), 370−378.
(67) Islam, S. M.; Im, J.; Freeman, A. J.; Kanatzidis, M. G. Ba2HgS5—A Molecular Trisulfide Salt with Dumbbell-like (HgS2)2- Ions. *Inorg. Chem.* **2014**, *53* (9), 4698−4704.
(68) Al-Gaashani, R.; Najjar, A.; Zakaria, Y.; Mansour, S.; Atieh, M. A. XPS and Structural Studies of High Quality Graphene Oxide and Reduced Graphene Oxide Prepared by Different Chemical Oxidation Methods. *Ceram. Int.* **2019**, *45* (11), 14439−14448.
(69) Ressler, T. Bulk Structural Investigation of the Reduction of MoO3 with Propene and the Oxidation of MoO2 with Oxygen. *J. Catal.* **2002**, *210* (1), 67−83.
(70) Manceau, A.; Marcus, M. A.; Grangeon, S. Determination of Mn Valence States in Mixed-Valent Manganates by XANES Spectroscopy. *Am. Mineral.* **2012**, *97* (5−6), 816−827.
(71) Islam, S. M.; Im, J.; Freeman, A. J.; Kanatzidis, M. G. Ba_2HgS_5 —A Molecular Trisulfide Salt with Dumbbell-like $(HgS_2)^{2-}$ Ions. *Inorg. Chem.* **2014**, *53* (9), 4698−4704.
(72) Kruglova, A. G. Tugarinovite, MoO_2, a New Hypogene Molybdenum Mineral. *International Geology Review* **1982**, *24* (5), 617−620.
(73) Martens, G.; Rabe, P.; Schwentner, N.; Werner, A. Improved Extended-x-Ray-Absorption Fine-Structure (EXAFS) Studies Applied to the Investigation of Cu-O, Cu-N, and Cu-Br Bond Lengths. *Phys. Rev. B* **1978**, *17* (4), 1481−1488.
(74) Hibble, S. J.; Wood, G. B. Modeling the Structure of Amorphous MoS_3: A Neutron Diffraction and Reverse Monte Carlo Study. *J. Am. Chem. Soc.* **2004**, *126* (3), 959−965.
(75) David, L.; Bhandavat, R.; Barrera, U.; Singh, G. Polymer-Derived Ceramic Functionalized MoS2 Composite Paper as a Stable Lithium-Ion Battery Electrode. *Sci. Rep* **2015**, *5* (1), 9792.
(76) Faizan, M.; Hussain, S.; Vikraman, D.; Ali, B.; Kim, H.-S.; Jung, J.; Nam, K.-W. MoS2@Mo2C Hybrid Nanostructures Formation as an Efficient Anode Material for Lithium-Ion Batteries. *Journal of Materials Research and Technology* **2021**, *14*, 2382−2393.
(77) Park, J.; Kim, J.-S.; Park, J.-W.; Nam, T.-H.; Kim, K.-W.; Ahn, J.-H.; Wang, G.; Ahn, H.-J. Discharge Mechanism of MoS2 for Sodium Ion Battery: Electrochemical Measurements and Characterization. *Electrochim. Acta* **2013**, *92*, 427−432.
(78) Wang, J.; Luo, C.; Gao, T.; Langrock, A.; Mignerey, A. C.; Wang, C. An Advanced MoS_2 /Carbon Anode for High-Performance Sodium-Ion Batteries. *Small* **2015**, *11* (4), 473−481.
(79) Feng, C.; Ma, J.; Li, H.; Zeng, R.; Guo, Z.; Liu, H. Synthesis of Molybdenum Disulfide (MoS2) for Lithium Ion Battery Applications. *Mater. Res. Bull.* **2009**, *44* (9), 1811−1815.
(80) Xiao, F.; Yang, X.; Wang, H.; Yu, D. Y. W.; Rogach, A. L. Hierarchical CoS_2 /N-Doped Carbon@MoS_2 Nanosheets with Enhanced Sodium Storage Performance. *ACS Appl. Mater. Interfaces* **2020**, *12* (49), 54644−54652.
(81) Matsuyama, T.; Hayashi, A.; Ozaki, T.; Mori, S.; Tatsumisago, M. Electrochemical Properties of All-Solid-State Lithium Batteries with Amorphous MoS_3 Electrodes Prepared by Mechanical Milling. *J. Mater. Chem. A* **2015**, *3* (27), 14142−14147.
(82) Li, Y.; Zhang, R.; Zhou, W.; Wu, X.; Zhang, H.; Zhang, J. Hierarchical MoS_2 Hollow Architectures with Abundant Mo Vacancies for Efficient Sodium Storage. *ACS Nano* **2019**, *13* (5), 5533−5540.
(83) Ye, W.; Wu, F.; Shi, N.; Zhou, H.; Chi, Q.; Chen, W.; Du, S.; Gao, P.; Li, H.; Xiong, S. Metal-Semiconductor Phase Twinned Hierarchical MoS_2 Nanowires with Expanded Interlayers for Sodium-Ion Batteries with Ultralong Cycle Life. *Small* **2020**, *16* (3), 1906607.

https://doi.org/10.1021/acsenergylett.3c02112
ACS Energy Lett. 2024, 9, 1−9